Article

Current Biology

Hippocampal engram networks for fear memory recruit new synapses and modify pre-existing synapses *in vivo*

Highlights

- Hippocampal synaptic connections are tracked by two-photon imaging of dual-eGRASP
- E-E synapses undergo synaptogenesis according to fear conditioning
- Extinction learning significantly correlated with the disappearance of E-E synapses
- Spatial distribution of new E-E synapses induces clustering of engram synapses

Authors

Chaery Lee, Byung Hun Lee, Hyunsu Jung, ..., Dong Il Choi, Hye Yoon Park, Bong-Kiun Kaang

Correspondence

hyp@umn.edu (H.Y.P.), kaang@snu.ac.kr (B.-K.K.)

In brief

Lee et al. use four-color two-photon imaging and dual-eGRASP system to enable longitudinal tracking of the synaptic connections between CA3 and CA1. From these data, they demonstrate a correlation between the dynamics of engram synapses and fear memory states. A particular distribution of newly formed synapses leads to clustering of E-E synapses.

Lee et al., 2023, Current Biology *33*, 507–516
February 6, 2023
https://doi.org/10.1016/j.cub.2022.12.038

CellPress

Current Biology

CellPress
OPEN ACCESS

Article

Hippocampal engram networks for fear memory recruit new synapses and modify pre-existing synapses *in vivo*

Chaery Lee,[1,5] Byung Hun Lee,[2,5] Hyunsu Jung,[1,3,5] Chiwoo Lee,[3] Yongmin Sung,[1] Hyopil Kim,[1] Jooyoung Kim,[1] Jae Youn Shim,[2] Ji-il Kim,[1] Dong Il Choi,[1] Hye Yoon Park,[2,4,*] and Bong-Kiun Kaang[1,3,6,*]

[1]Department of Biological Sciences, College of Natural Sciences, Seoul National University, Seoul 08826, South Korea
[2]Department of Physics and Astronomy, College of Natural Sciences, Seoul National University, Seoul 08826, South Korea
[3]Interdisciplinary Program in Neuroscience, Seoul National University, Seoul 08826, South Korea
[4]Department of Electrical and Computer Engineering, College of Science and Engineering, University of Minnesota, Minneapolis, MN 55455, USA
[5]These authors contributed equally
[6]Lead contact
*Correspondence: hyp@umn.edu (H.Y.P.), kaang@snu.ac.kr (B.-K.K.)
https://doi.org/10.1016/j.cub.2022.12.038

SUMMARY

As basic units of neural networks, ensembles of synapses underlie cognitive functions such as learning and memory. These synaptic engrams show elevated synaptic density among engram cells following contextual fear memory formation. Subsequent analysis of the CA3-CA1 engram synapse revealed larger spine sizes, as the synaptic connectivity correlated with the memory strength. Here, we elucidate the synapse dynamics between CA3 and CA1 by tracking identical synapses at multiple time points by adapting two-photon microscopy and dual-eGRASP technique *in vivo*. After memory formation, synaptic connections between engram populations are enhanced in conjunction with synaptogenesis within the hippocampal network. However, extinction learning specifically correlated with the disappearance of CA3 engram to CA1 engram (E-E) synapses. We observed "newly formed" synapses near pre-existing synapses, which clustered CA3-CA1 engram synapses after fear memory formation. Overall, we conclude that dynamics at CA3 to CA1 E-E synapses are key sites for modification during fear memory states.

INTRODUCTION

Memory engrams reflect the population of neurons activated during memory formation.[1–3] Reactivation or inactivation of these engram cells correlates with the recall or inhibition of the memory retrieval, respectively.[1,3,4] Evidence shows that the synapses of these engram cells physically encode the memory trace, implying that the synaptic networks between engram cells underlie memory formation, maintenance, and extinction.[5–7] Indeed, specifically enhanced synaptic connections between CA3 engram cells and CA1 engram cells were observed using "dual-eGRASP"[8] that labels the presynaptic and postsynaptic part of GFP contacts.[9,10] The correlation of memory states and the synapses between engram cells reflect alterations in the spine morphology of activated neuronal ensembles.[11] Further, the localization of synapses within a dendritic branch is critical in memory formation throughout the brain.[12–14] Randomly scattered synapses primarily occur in sensory cortices, while synapses cluster in several other brain areas,[12,13] which may indicate hotspots of dendritic spines with enhanced turnover rates.[14] Whether such clustered spine formation is specific to engram synapses still remains an open question.

Technical limitations constrained prior studies to observations in different subjects at a specific memory state. Since the dual-eGRASP signals were obtained from perfused brain slices, longitudinal imaging within identical subjects was impossible. This technical approach hampered investigations on the dynamic changes in synaptic connectivity during various memory states *in vivo*. To overcome these issues, we integrated four-color *in vivo* two-photon imaging and dual-eGRASP system. Using this advanced approach, we sought to uncover the synaptic mechanisms that underlie engram synapse-specific enhanced connectivity during memory formation and the synaptic distributions on dendrites by comparing identical synapses across different memory states. Our analysis of synaptic dynamics between connected engram cells revealed (1) a higher proportion of "newly formed" synapses on postsynaptic engram dendrites, (2) a significant decrease in "E-E" synapses after memory extinction, and (3) a close distribution of newly formed synapses in sparsely innervated dendritic areas and clustering of E-E synapses.

RESULTS

In vivo two-photon imaging enables longitudinal observation of dual-eGRASP in CA1

Using adeno-associated virus (AAV), we expressed dual-eGRASP,[8] which can label synapses with spectrally different fluorescence proteins (cyan and yellow) according to presynaptic motifs (Figure 1A, left). To monitor random CA1 postsynaptic dendrites, we induced a sparse and constitutive expression of

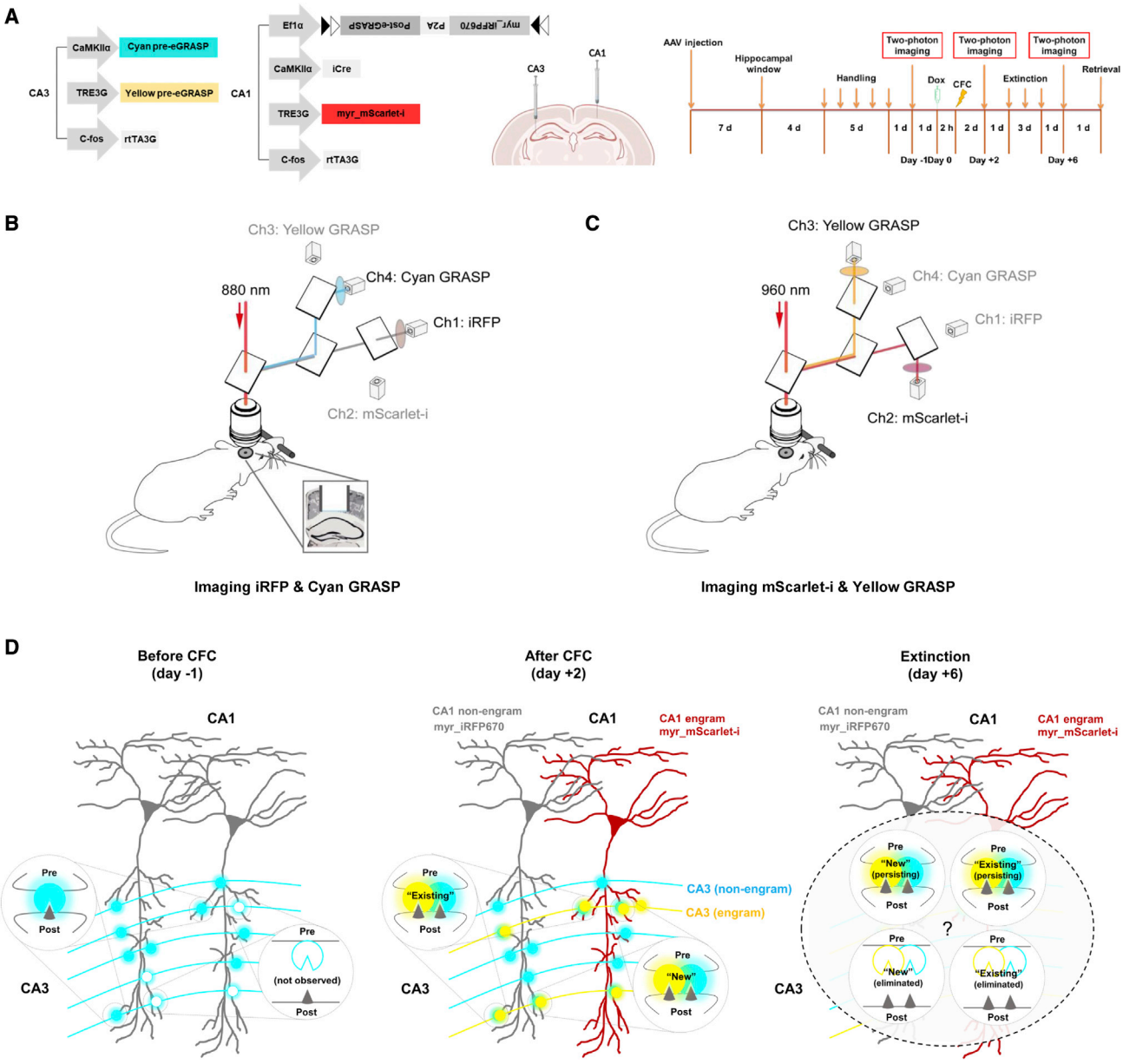

Figure 1. Experimental strategy diagrams to image synaptic connections *in vivo*

(A) Left: schematic illustration of AAVs injected into CA3 and CA1 of the hippocampus. Middle: virus cocktails were injected into contralateral CA3 and ipsilateral CA1 of the hippocampus. Right: schematic illustration of the experimental protocol to examine synaptic connections through memory formation and extinction.

(B) Using an excitation wavelength of 880 nm, cyan GRASP and random apical dendrites of CA1 (iRFP) were observed through the hippocampal window (inset). Fluorescence intensity was determined via different PMTs after passing through dichroic mirrors and band-pass filters.

(C) Yellow GRASP and apical dendrite of engram neurons in CA1 (mScarlet-i) were imaged using excitation wavelengths of 960 nm.

(D) Schematic illustration of synapse classification based on their existence and persistence in each memory state.

iRFP670 and post-eGRASP. To visualize CA1 engram dendrites at specific time points, we expressed myristoylated mScarlet-i driven by the Fos-dependent reverse tetracycline transactivator (Fos-rtTA).[15–18] We induced a dense expression of cyan pre-eGRASP without Cre recombinase to cover most of the excitatory presynaptic inputs from contralateral CA3. To label synaptic inputs from a contralateral CA3 engram cell to CA1 neurons (Figure 1A, middle), we expressed yellow pre-eGRASP using the Fos-rtTA system. These expression patterns enabled identifying CA3 engram to CA1 engram (E-E) synapses, which are recognized by yellow eGRASP signals on mScarlet-i expressing dendrites. Similarly, based on CA1 dendritic expression of mScarlet-i and the presence of yellow GRASP on CA1 spines, we classified synapses into four classes between presynaptic and postsynaptic engram (E) and non-engram (N) cells: E-E, N-E, E-N, and N-N.

After 7 days of recovery following AAV injection, hippocampal windows were implanted above dorsal CA1. After ~14–16 days

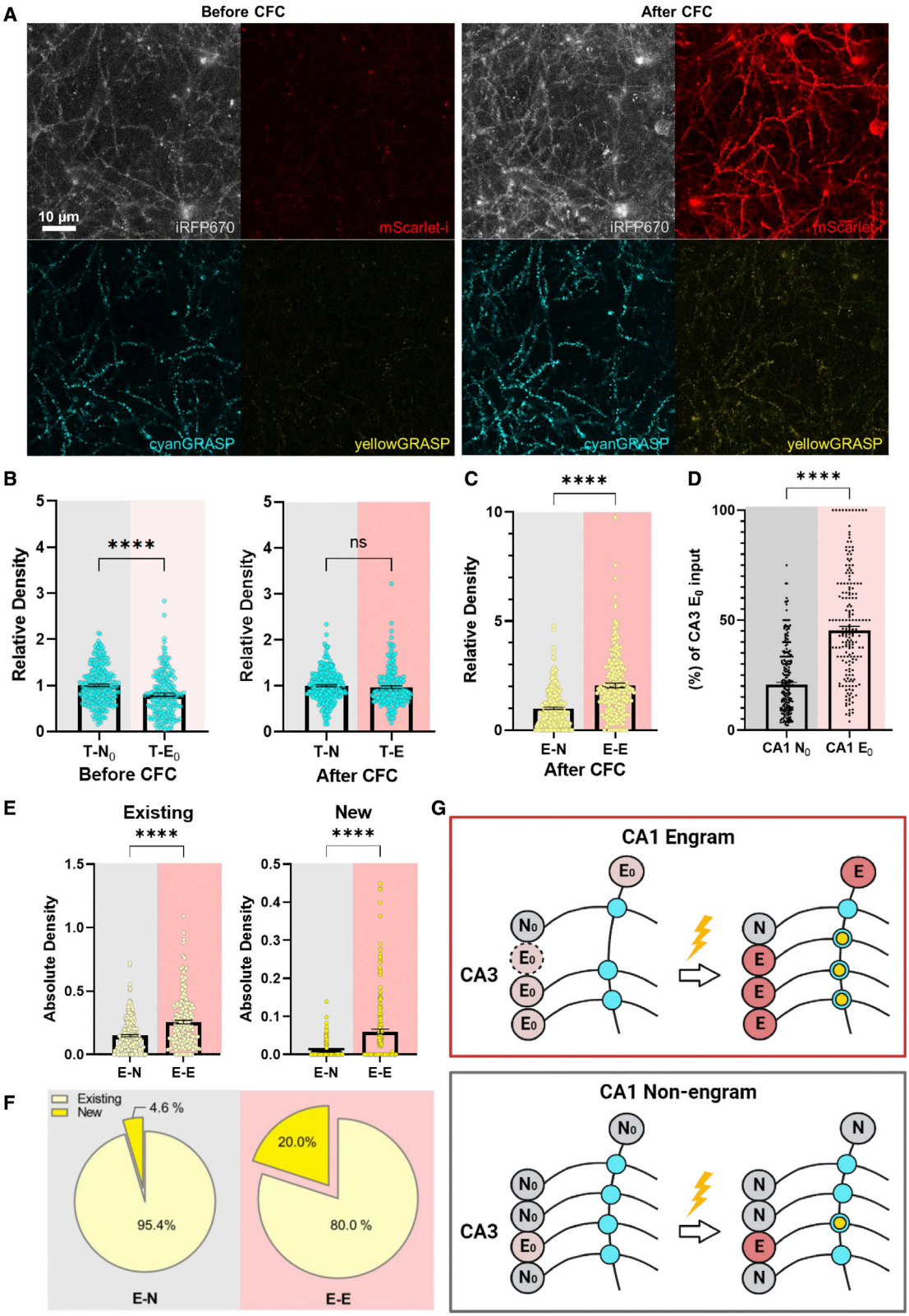

(legend on next page)

of AAV expression, we conducted *in vivo* two-photon imaging of dual-eGRASP signals in the mouse CA1 before and after contextual fear conditioning (CFC) and after fear extinction (Figure 1A, right; Figure S2A). Four types of fluorescence proteins (cyan eGRASP, yellow eGRASP, mScarlet-i, and iRFP670) were imaged with an excitation laser tuned at two different wavelengths (Figures 1B and 1C).

Identical CA1 pyramidal cell dendrites were tracked by two-photon imaging in multiple areas of CA1 (Figure 1D), and the images were further processed to reduce motion artifacts and to improve the resolution by deconvolution. Before fear conditioning, constitutively expressed cyan eGRASP covered most of the existing excitatory synapses in the CA3 to CA1 circuit. Thus, in terms of synapse dynamics, we could investigate whether a synapse was newly formed after fear conditioning or already existed by comparing the cyan eGRASP signals before CFC, after CFC, and after fear extinction. Combining this turnover information with engram synapse classification, we could map the persistence of engram synapses upon fear conditioning and extinction. Further, we could reveal if the increased synaptic density of E-E synapses derived from newly formed or "existing" synapses. In addition, we could analyze if each synapse was persistent or eliminated using the two-photon images taken after fear extinction.

New synapses form primarily at E-E connections during memory formation

From the two-photon images of mouse CA1, we observed four kinds of synapses formed between CA3 and CA1 non-engram or engram (Figures 2A and 2B). "Cyan only" synapses on the non-engram dendrites labeled only by iRFP670 represented N-N, while those on the engram dendrites that were labeled with both iRFP670 and mScarlet-i represented N-E. Moreover, "yellow only" and "cyan + yellow" synapses on the non-engram dendrites represented E-N, while those on the engram dendrites represented E-E. Only few synapses were labeled as yellow only after memory formation, suggesting that cyan eGRASP already covered most of the existing synapses. By manually comparing the dual-eGRASP signals of these four types of synapses at our three time points (before memory formation, after memory formation, and after fear extinction), we could investigate the synaptic dynamics in more detail.

We first observed an elevated relative synaptic density of E-E connections compared with E-N after fear memory formation, reproducing our previous report[8] (Figure 2C). The synaptic density of total presynaptic cells to the engram (T-E) was significantly lower than that of T-N before fear conditioning (Figure 2B, left). However, no differences between T-N and T-E were found after memory formation, consistent with the previous data[8] (Figure 2B, right; Figure S1). These confirmatory data indicate that engram synapses preferentially form on dendrites with lower density of synaptic inputs from CA3. Our advanced methodology for *in vivo* eGRASP did not significantly impact our previous results. We next examined the dendritic proportion of synaptic inputs that CA1 dendrites receive from CA3 cells (E_0) before fear conditioning that eventually become engrams after fear conditioning. CA1 E_0 dendrites received a significantly higher percentage of inputs from CA3 E_0 neurons compared with N_0 dendrites that still remained non-engrams after fear conditioning (Figure 2D). Moreover, to elucidate whether the increased synaptic density was derived from existing or newly formed synapses, we tracked the history of dual-eGRASP signals of synapses on either non-engram or engram dendrites labeled as cyan + yellow after memory formation. Interestingly, both existing and newly formed synapses accounted for the elevated synaptic density of the E-E connection (Figure 2E). However, the proportion of newly formed synapses was significantly higher in engram dendrites than that in non-engram dendrites, indicating that newly formed synapses may exert a greater contribution for memory formation at the synaptic level in memory engram networks (Figure 2F). Such synaptic dynamics were not observed when the mice only underwent context exposure without any conditioning (Figure S3). In conclusion, CA1 engram dendrites are preferentially connected with CA3 engram cells even before fear conditioning, while CA1 non-engram dendrites receive unbiased inputs from CA3 neurons. Interestingly, some neurons with dendrites receiving less excitatory synapses were recruited as engram dendrites due to the major input from CA3 potential engram cells (Figure 2G).

E-E synapses significantly decrease after memory extinction

To examine changes at the synaptic level according to memory attenuation, we tracked identical spines after fear memory

Figure 2. Elevated existing and newly formed synaptic populations in CA1 engram dendrites after CFC

(A) Representative two-photon images of dual-eGRASP signals in a non-engram or engram dendrite before and after CFC.

(B) Relative density of random cyan GRASP on non-engram or engram dendrites before and after fear conditioning; CA1 non-engram dendrites (n = 199); CA1 engram dendrites (n = 266); Mann-Whitney two-tailed test. Left, before CFC: ****$p < 0.0001$. Right, after CFC: $p = 0.4377$. N_0 and E_0 indicate CA1 cells before CFC that become non-engram and engram later after CFC, respectively.

(C) Relative density of yellow GRASP on non-engram or engram dendrites after fear conditioning; CA1 non-engram dendrites (n = 199); CA1 engram dendrites (n = 266); Mann-Whitney two-tailed test. ****$p < 0.0001$.

(D) Dendritic proportion of synaptic inputs from CA3 E_0 before CFC. The ratio of particular cyan eGRASP, tracked as cyan + yellow eGRASP after CFC among total cyan eGRASP, was measured; CA1 N_0 dendrites (n = 199); CA1 E_0 dendrites (n = 266); Mann-Whitney two-tailed test. ****$p < 0.0001$.

(E) The absolute densities of existing or newly formed synapses. CA1 non-engram dendrites (n = 199); CA1 engram dendrites (n = 266); (left) Mann-Whitney two-tailed test. ***$p < 0.0001$; (right) Mann-Whitney two-tailed test. ***$p < 0.0001$.

(F) The proportion of existing and newly formed synapses in non-engram or engram dendrites; existing N-E synapses (n = 1,122); new N-E synapses (n = 54); existing E-E synapses (n = 1,245); new E-E synapses (n = 311); CA1 non-engram dendrites (n = 199); CA1 engram dendrites (n = 266).

(G) Schematic illustration of the overall synaptic dynamics between CA3 and CA1 neurons before and after CFC. Upper box, CA1 engram; lower box, CA1 non-engram. Circles entitled as N_0 and E_0 indicate CA3 and CA1 neurons that were each labeled as non-engram and engram after CFC, respectively. E_0 with a dotted circle indicates CA3 neuron whose presence remains unknown. Circles on crossed lines indicate cyan GRASP or cyan and yellow GRASP.

Data are represented as mean ± SEM in all figures. See also Figures S1–S3.

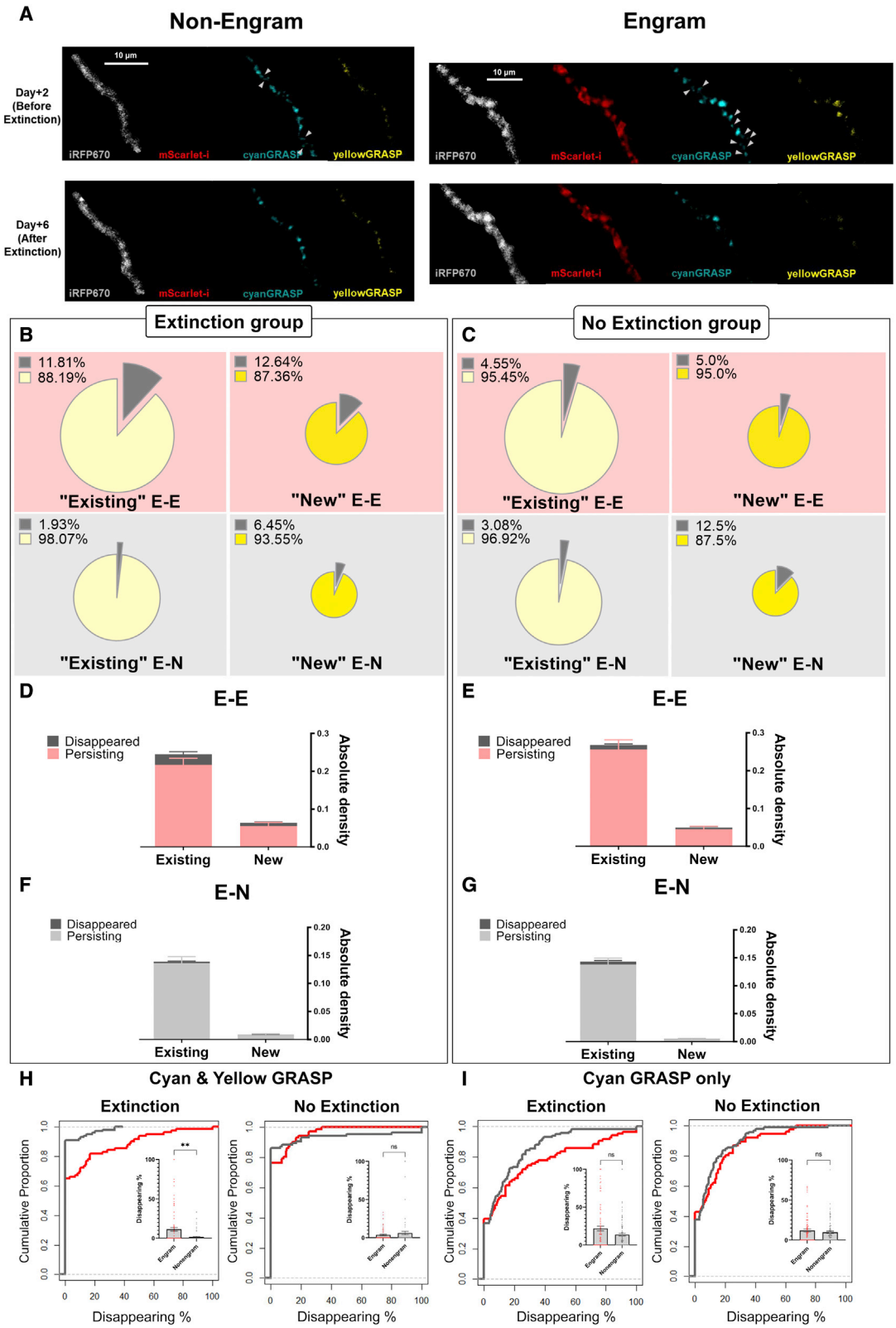

Figure 3. Extinction eliminates both existing and new engram-engram synapses

(A) Representative image of engram and non-engram dendrites after fear extinction training. Arrows indicate dual-eGRASP signals that disappeared after fear extinction. See also Figure S3.

(legend continued on next page)

extinction (Figures S2C and S2D). Particularly, we observed the dynamics of synapses labeled as cyan + yellow after CFC on either CA1 engram or non-engram cells. Dendrites that were previously selected for analysis after memory formation were analyzed again, and we determined whether each dual-eGRASP signal remained or completely disappeared from the two-photon images (Figure 3A). Since cyan GRASP was constitutively expressed during the experiment, some of the cyan only synapses were also generated or disappeared after fear extinction. So, we tracked "total cyan" GRASP signals, which included both cyan only and cyan + yellow, during the entire experiment. The relative spine density of total cyan GRASP synapses was significantly increased after fear memory formation, while we could not observe any significant changes after fear extinction (Figure S1).

From our analysis of two-photon images taken after fear extinction, we first observed the disappearance of either "new" or existing E-E synapses, which both occurred approximately at a frequency of 12% (Figure 3B). Compared with E-N synapses, a significantly higher percentage of existing E-E synapses disappeared (Figure S4). Interestingly, the decrease of absolute spine density due to the disappearance of some synapses was limited to E-E synapses, while nearly none of the E-N synapses disappeared (Figures 3D and 3F). Such E-E specific disappearance of existing synapses occurred only when the subjects underwent fear extinction, as E-E and E-N synapses showed insignificant differences in the no extinction group (Figures 3C, 3E, and 3G). Disappearance of synapses from CA3 engrams was biased to CA1 engram dendrites by extinction training, while synapses from CA3 non-engrams did not show any significant differences (Figures 3H and 3I). Repeated context exposure did not induce any particular disappearance of synapses (Figures S3F–S3H). Based on these data, we propose that contextual fear memory is highly correlated with the alteration of CA3-CA1 E-E synapses during memory attenuation.

Spatial distribution of newly formed E-E synapses cluster E-E synapses

Synapses are distributed in a scattered pattern on dendrites, which is determined by their anatomical structures.[19] However, another proposal claims that the clustering of dendritic spines with various spine morphologies also pre-determines the general location of synapses.[20] Here, we examined whether the newly formed spines elicited by CFC showed a particular pattern of spatial distribution. First, we analyzed the dendritic spines labeled with dual-eGRASP at a spine level (Figure 4A). Given the longitudinal images of synapses and dendrites, we could identify three-dimensional coordinates of synapses and measure the distance between each class of synapses. Even though both E-E and N-E synapses were newly formed after memory formation, only the mean distance between new E-E synapses was significantly shorter than the overall average distance of random synapses (Figure 4B). This indicated that the new E-E synapses are closely formed with each other compared with other types of synapses.

We further visualized the distribution of existing and newly formed synapses by projecting the dual-eGRASP signals on a one-dimensional graph. We found that new synapses (red circles in Figure 4C) were closely formed in some dendritic regions with significantly lower spine density (Figures 4C and 4D). The E-E synapses generated after fear memory formation tended to locate on sparser dendritic areas with higher capacity. Newly formed E-E synapses were significantly paired with existing E-E synapses rather than with existing N-E synapses (Figure 4E). Thus, E-E synapses form near existing E-E synapses after fear memory formation. Moreover, the average nearest neighbor distance (NND) of total E-E synapses was significantly smaller than random chance (Figure 4G), while that of existing E-E synapses was comparable to a chance level (Figure 4F). Such data indicate that the formation of new E-E synapses near dispersed existing E-E synapses resulted in the clustering of E-E synapses after memory formation. Such learning-related distribution of spines is known to occur within dendritic segments with increased spine turnover, which also increases network sparsity and memory capacity in the retrosplenial cortex.[13] Thus, these data indicate that new E-E synapses could also form within the dendritic hotspots.

DISCUSSION

Here, we adapted two-photon imaging with the dual-eGRASP system, enabling us to track the same synapse on specific

(B) Proportions of persisting and disappearing engram synapses in the extinction group. Yellow and gray indicate persisting and disappeared percentages of the synapses, respectively. Disappeared existing E-E synapses (n = 75); persisting existing E-E synapses (n = 560); disappeared new E-E synapses (n = 22); persisting new E-E synapses (n = 152); disappeared existing E-N synapses (n = 10); persisting existing E-N synapses (n = 507); disappeared new E-N synapses (n = 2); persisting new E-N synapses (n = 29).
(C) Proportions of persisting and disappearing engram synapses in the no extinction group. Yellow and gray indicate persisting and disappeared percentages of the synapses, respectively. Disappeared existing E-E synapses (n = 23); persisting existing E-E synapses (n = 482); disappeared new E-E synapses (n = 5); persisting new E-E synapses (n = 95); disappeared existing E-N synapses (n = 13); persisting existing E-N synapses (n = 409); disappeared new E-N synapses (n = 2); persisting new E-N synapses (n = 14).
(D) Absolute synaptic density of existing and new E-E synapses in the extinction group. CA1 engram dendrites (n = 86); CA1 non-engram dendrites (n = 117).
(E) Composition of existing and new E-E synapses in the no extinction group. CA1 engram dendrites (n = 78); CA1 non-engram dendrites (n = 98).
(F) Absolute synaptic density of existing and new E-N synapses in the extinction group. CA1 engram dendrites (n = 86); CA1 non-engram dendrites (n = 117).
(G) Absolute synaptic density of existing and new E-N synapses in the no extinction group. CA1 engram dendrites (n = 78); CA1 non-engram dendrites (n = 98).
(H) Cumulative plot of disappearing percentage of E-E or E-N synapses on CA1 dendrites of extinction and no extinction group. CA1 engram dendrites of extinction group (n = 86); CA1 non-engram dendrites of extinction group (n = 117); CA1 engram dendrites of no extinction group (n = 78); CA1 non-engram dendrites of no extinction group (n = 98); Kolmogorov-Smirnov test, extinction, p = 0.0039; no extinction, p = 0.7305.
(I) Cumulative plot of disappearing percentage of N-E or N-N synapses on CA1 dendrites of extinction and no extinction group. CA1 engram dendrites of extinction group (n = 86); CA1 non-engram dendrites of extinction group (n = 117); CA1 engram dendrites of no extinction group (n = 78); CA1 non-engram dendrites of no extinction group (n = 98); Kolmogorov-Smirnov test, extinction, p = 0.1989; no extinction, p = 0.4428.
Data are represented as mean ± SEM in all figures. See also Figures S2–S4.

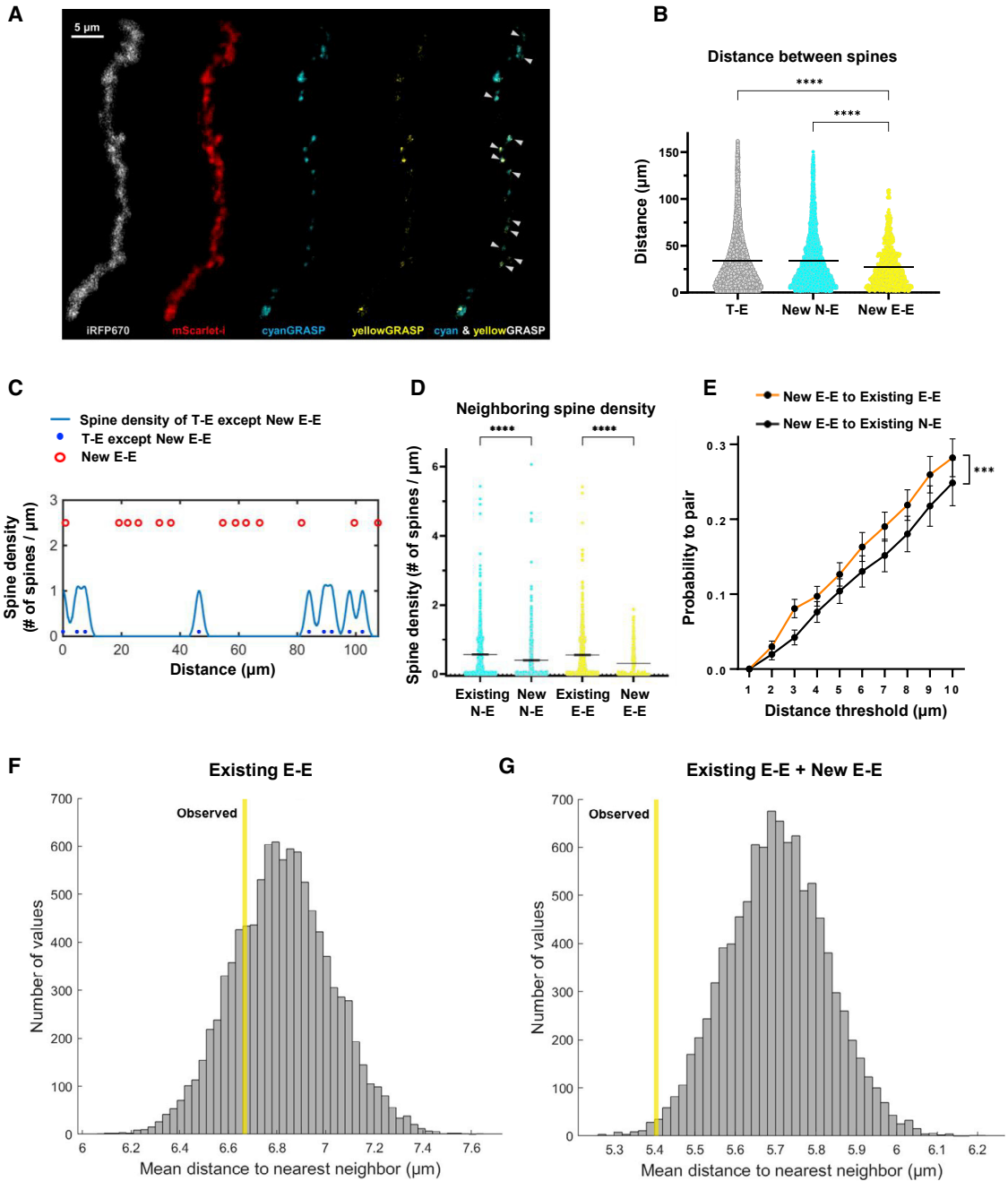

Figure 4. Dendritic distribution of synaptic connections among engram cells

(A) Representative image of the spatial distribution of newly formed E-E synapses on CA1 engram dendrite. Arrows indicate newly formed E-E synapses.

(B) Distances measured between spines within identical categories. Each dot indicates distance measured between two random spines within a dendrite segment. Pairs of new E-E synapses (n = 952); pairs of new N-E synapses (n = 5262); pairs of T-E synapses (n = 66436); Dunn's multiple comparisons test after Kruskal-Wallis test. Kruskal-Wallis, ****$p < 0.0001$; Dunn's, ****$p < 0.0001$.

(C) Spine density histogram (light blue) and one-dimensional plotted spines (blue)/newly formed E-E spines (red) on a representative dendrite.

(D) Spine densities (spine number = 2.5 μm) measured at the dendritic locations of four different types of synapses. Each dot indicates surrounding spine density that was measured by the number of spines within a 2.5 μm-wide moving window. Density of surrounding "pre-existing" N-E and E-E synapses was calculated. Existing N-E synapses (n = 1,003); new N-E synapses (n = 655); existing E-E synapses (n = 841); new E-E synapses (n = 230); Dunn's multiple comparisons test after Kruskal-Wallis test. Kruskal-Wallis, ****$p < 0.0001$; Dunn's, ****$p < 0.0001$. Data are represented as mean ± SEM in all figures.

(E) The number of pairs between two groups of synapses existing within various distance thresholds divided by the total number of possible pairs selected between two groups of synapses. "New E-E to existing E-E" indicates the pairs between newly formed E-E synapses and existing E-E synapses (n = 76); new E-E

(legend continued on next page)

dendrites over time *in vivo*. Since two-photon imaging permitted measurements at multiple time points, we could analyze the changing synaptic dynamics occurring in different memory states induced by fear memory formation or extinction. Engram-specific features at a synaptic level have been previously researched by adapting the dual-eGRASP system. Spine density and morphologies at synaptic connections between CA3 engrams and CA1 engrams significantly increase after fear memory formation.[8] However, limitations with confocal imaging using the dual-eGRASP system necessitated using a single animal and restricted time points to visualize the synapses. Since the data were obtained from different individuals, observing the actual changes occurring in an identical subject *in vivo* was impossible. Our newly developed method overcomes these challenges.

Since motor or auditory fear memory formation can generate new spines,[21–23] we predicted that newly formed synapses would underlie the elevated synaptic density at the E-E synaptic connection. We found that newly formed synapses accounted for a relatively high proportion of the elevated synaptic density in CA1 engram dendrites. Yet we also found that the absolute spine density of existing synapses was also significantly higher in CA1 engram dendrites. Thus, memory formation requires both new and modified pre-existing synapses. We propose that newly formed synapses support the modifications to existing synapses to expand engram memory networks. This then raises the question of which cells have the potential to become engram cells. Based on our data, we posit that cells with lower spine density and higher memory capacity have a higher probability to become engram cells by forming new synapses and possibly increasing the neuronal inputs from the connections and excitability. Surprisingly, we found that such cells from CA3 and CA1 appeared to be connected to each other even before memory formation unlike the allocation theory in which neurons with fluctuating excitability are recruited as engram. These data implicated that recruitment for memory trace might be rather based on the pre-existing connectivity between neurons.

Two mechanisms have been proposed to underlie fear memory extinction—"unlearning" of pre-acquired memories and "new learning" about the contingency.[24,25] A recent study demonstrated that newly formed spines in the auditory cortex during the auditory fear conditioning were eliminated upon extinction of that memory.[26] Specifically, the enhanced spine morphology in the lateral amygdala was weakened following fear memory extinction.[11] While our previous study focused on the changes of spine morphology in the auditory cortex to the lateral amygdala circuit, we examined the dynamics of synaptic density in the hippocampus by using our fear conditioning paradigm and a new method. We found that some E-E synapses were eliminated following fear memory extinction. These data would support the unlearning hypothesis. Since both newly formed and existing synapses are vulnerable to memory extinction, we suspect that these E-E synapses within the dorsal hippocampus are correlated with fear memory traces. By utilizing our experimental scheme on various brain regions, whether the mechanism is universal could be further elucidated.

Finally, our data indicate that newly formed synapses are closely distributed in particular dendritic areas with lower spine density. Although the distance between these new E-E synapses was relatively shorter, the distance between other existing E-E synapses or cyan only N-E synapses was relatively longer. In addition, newly formed E-E synapses were closely distributed with existing E-E synapses. New spines in the motor cortex form during learning nearby pre-existing spines that exhibited task-related activity.[27] Since longitudinal two-photon imaging enabled distinguishing new E-E synapses from existing E-E synapses, we speculated that such learning-related events also occur at the E-E synapse level. Thus, we observed how learning induces the clustering of synaptic engrams in the dorsal hippocampus *in vivo*.

Clustering of spines is well known to affect physiological properties in cortical areas. For instance, by enabling synaptic tagging and capturing, clustered plasticity is known to convert E-LTP/E-LTD to L-LTP/L-LTD.[28] Moreover, synaptic plasticity mediated by an NMDA receptor is crucial for hippocampal spatial memory.[29] Clustered synapses are presumed to induce local dendritic spikes mediated by NMDA receptors, even in the absence of somatic action potential firing.[30] Such correlation between spine clustering and biological properties has also been observed in the hippocampus. For instance, structural plasticity of L-LTP was inversely proportional to the distance between dendritic spines within CA1 *ex vivo* slices.[31] Plasticity-related protein products (PrPs) were highly shared between spines with shorter distance less than 50 μm.[31] Thus, the shorter mean distance between newly formed synaptic engrams in Figure 4B implies that those synapses contribute to clustered plasticity. We posit that new hippocampal memory clusters CA3 to CA1 E-E synapses after incorporating synapses that existed before learning. However, further studies should elucidate the functional and physiological relevance of clustering of newly formed synapses *in vivo*.

In this study, we also encountered several limitations in this *in vivo* dual-eGRASP approach. First, color schemes for the labeling of CA1 engram and non-engram dendrites were limited since two channels of two-photon microscopy were occupied by cyanGRASP and yellowGRASP. Such technical limitation led us to use the constitutive expression of iRFP670 in random CA1 dendrites. On our current two-photon microscopy setup, iRFP670 appeared to be extremely blur and vulnerable to bleaching. Thus, it was difficult to analyze additional data related to spine morphology such as spine size or volume from CA1 dendrites. Moreover, tracking dendritic spines in real time via *in vivo* live imaging was hindered due to the motions caused by breathing of mice during imaging. Motion correction and image processing were required for GRASP analysis even though two-photon images were acquired from anesthetized mice. Further studies with two-photon imaging of awake mice would require advanced image stabilization for spine-level analysis.

to existing N-E indicates the pairs between newly formed E-E synapses and existing N-E synapses (n = 69); two-way ANOVA; distance threshold, $F(9, 1,430) = 47.29$, ****$p < 0.0001$; type of synapse pair, $F(1, 1,430) = 11.43$, ***$p < 0.001$; interaction, $F(9, 1,430) = 0.2900$, $p = 0.9777$.

(F and G) Null distribution of the average nearest neighbor distance (NND) from existing E-E synapses (F) and total E-E synapses (G). 10,000 simulations of randomized label of spines were run, while the coordinates and number of each label of spines were controlled. Yellow line indicates the actual average NND (6.67 μm in existing E-E synapses, 5.40 μm in total E-E synapses) observed in the data.

Moreover, additional studies will be required for functional manipulation of E-E synapses. Revealing the causal relation between the dynamics of specific spines and learning and memory still remains as a challenge.

Despite these limitations, we elucidated the synaptic dynamics in CA1 by combining longitudinal *in vivo* two-photon imaging with dual-eGRASP for the first time. Our findings successfully advance previous studies by enabling the classification of E-E synapses according to their existence before fear memory formation. Thus, we demonstrate that synaptic connections between engram cells specifically accompany synaptogenesis. These connections are also preferentially influenced by memory extinction. Furthermore, theoretical studies have proposed that clustered plasticity may be crucial for memory storage. Our data imply that clustering may occur at interregional engram populations that undergo synaptogenesis induced by memory formation. In conclusion, our results strongly support the hypothesis that Schaffer collateral E-E synapses are the physical substrates of fear memory traces.

STAR★METHODS

Detailed methods are provided in the online version of this paper and include the following:

- KEY RESOURCES TABLE
- RESOURCE AVAILABILITY
  - Lead contact
  - Materials availability
  - Data and code availability
- EXPERIMENTAL MODEL AND SUBJECT DETAILS
  - Mice
- METHOD DETAILS
  - AAV virus production
  - Stereotaxic surgery
  - Hippocampal window surgery
  - Contextual fear conditioning and extinction
  - Sample preparation and confocal imaging
  - *In vivo* two-photon imaging
  - Image processing
  - IMARIS analysis
  - Spine distribution analysis
- QUANTIFICATION AND STATISTICAL ANALYSIS

SUPPLEMENTAL INFORMATION

Supplemental information can be found online at https://doi.org/10.1016/j.cub.2022.12.038.

ACKNOWLEDGMENTS

This work was supported by the National Honor Scientist Program (NRF-2012R1A3A1050385) of Korea. B.H.L., J.Y.S., and H.Y.P. were supported by the Samsung Science and Technology Foundation under project number SSTF-BA1602-11 and the Basic Science Research Program through the National Research Foundation of Korea (NRF) (2020R1A2C2007285).

AUTHOR CONTRIBUTIONS

Conceptualization, H.K., Chaery Lee, H.J., and B.-K.K.; methodology, H.K., B.H.L., Chaery Lee, and H.J.; software, B.H.L., Chiwoo Lee, and Y.S.; formal analysis, Chaery Lee, H.J., B.H.L., Chiwoo Lee, Y.S., and J.K.; investigation, Chaery Lee, H.J., and Y.S.; resources, J.-i.K. and D.I.C.; writing, Chaery Lee, B.H.L., H.Y.P., and B.-K.K.; supervision, H.Y.P. and B.-K.K.; funding acquisition, H.Y.P. and B.-K.K.

DECLARATION OF INTERESTS

The authors declare no competing interests.

Received: September 19, 2022
Revised: December 7, 2022
Accepted: December 14, 2022
Published: January 12, 2023

REFERENCES

1. Ramirez, S., Liu, X., Lin, P.A., Suh, J., Pignatelli, M., Redondo, R.L., Ryan, T.J., and Tonegawa, S. (2013). Creating a false memory in the hippocampus. Science *341*, 387–391. https://doi.org/10.1126/science.1239073.
2. Semon, R.W., and Simon, L. (1921). The Mneme (Macmillan).
3. Liu, X., Ramirez, S., Pang, P.T., Puryear, C.B., Govindarajan, A., Deisseroth, K., and Tonegawa, S. (2012). Optogenetic stimulation of a hippocampal engram activates fear memory recall. Nature *484*, 381–385. https://doi.org/10.1038/nature11028.
4. Han, D.H., Park, P., Choi, D.I., Bliss, T.V.P., and Kaang, B.K. (2022). The essence of the engram: cellular or synaptic? Semin. Cell Dev. Biol. *125*, 122–135. https://doi.org/10.1016/j.semcdb.2021.05.033.
5. Lacagnina, A.F., Brockway, E.T., Crovetti, C.R., Shue, F., McCarty, M.J., Sattler, K.P., Lim, S.C., Santos, S.L., Denny, C.A., and Drew, M.R. (2019). Distinct hippocampal engrams control extinction and relapse of fear memory. Nat. Neurosci. *22*, 753–761. https://doi.org/10.1038/s41593-019-0361-z.
6. Hayashi-Takagi, A., Yagishita, S., Nakamura, M., Shirai, F., Wu, Y.I., Loshbaugh, A.L., Kuhlman, B., Hahn, K.M., and Kasai, H. (2015). Labelling and optical erasure of synaptic memory traces in the motor cortex. Nature *525*, 333–338. https://doi.org/10.1038/nature15257.
7. Abdou, K., Shehata, M., Choko, K., Nishizono, H., Matsuo, M., Muramatsu, S.I., and Inokuchi, K. (2018). Synapse-specific representation of the identity of overlapping memory engrams. Science *360*, 1227–1231. https://doi.org/10.1126/science.aat3810.
8. Choi, J.H., Sim, S.E., Kim, J.I., Choi, D.I.I., Oh, J., Ye, S., Lee, J., Kim, T., Ko, H.G., Lim, C.S., and Kaang, B.K. (2018). Interregional synaptic maps among engram cells underlie memory formation. Science *360*, 430–435. https://doi.org/10.1126/science.aas9204.
9. Kim, J., Zhao, T., Petralia, R.S., Yu, Y., Peng, H., Myers, E., and Magee, J.C. (2011). MGRASP enables mapping mammalian synaptic connectivity with light microscopy. Nat. Methods *9*, 96–102. https://doi.org/10.1038/nmeth.1784.
10. Feinberg, E.H., VanHoven, M.K., Bendesky, A., Wang, G., Fetter, R.D., Shen, K., and Bargmann, C.I. (2008). GFP reconstitution across synaptic partners (GRASP) defines cell contacts and synapses in living nervous systems. Neuron *57*, 353–363. https://doi.org/10.1016/j.neuron.2007.11.030.
11. Choi, D.I., Kim, J., Lee, H., Kim, J.I., Sung, Y., Choi, J.E., Venkat, S.J., Park, P., Jung, H., and Kaang, B.K. (2021). Synaptic correlates of associative fear memory in the lateral amygdala. Neuron *109*, 2717–2726.e3. https://doi.org/10.1016/j.neuron.2021.07.003.
12. Kastellakis, G., and Poirazi, P. (2019). Synaptic clustering and memory formation. Front. Mol. Neurosci. *12*, 300. https://doi.org/10.3389/fnmol.2019.00300.
13. Frank, A.C., Huang, S., Zhou, M., Gdalyahu, A., Kastellakis, G., Silva, T.K., Lu, E., Wen, X., Poirazi, P., Trachtenberg, J.T., and Silva, A.J. (2018). Hotspots of dendritic spine turnover facilitate clustered spine addition and learning and memory. Nat. Commun. *9*, 422. https://doi.org/10.1038/s41467-017-02751-2.

14. Van Ooyen, A., and Butz-Ostendorf, M. (2017). The Rewiring Brain: A Computational Approach to Structural Plasticity in the Adult Brain (Academic Press).
15. van Haasteren, G., Li, S., Ryser, S., and Schlegel, W. (2000). Essential contribution of intron sequences to Ca$^{(2+)}$-dependent activation of c-fos transcription in pituitary cells. Neuroendocrinology *72*, 368–378. https://doi.org/10.1159/000054606.
16. Loew, R., Heinz, N., Hampf, M., Bujard, H., and Gossen, M. (2010). Improved Tet-responsive promoters with minimized background expression. BMC Biotechnol. *10*, 81. https://doi.org/10.1186/1472-6750-10-81.
17. Reijmers, L.G., Perkins, B.L., Matsuo, N., and Mayford, M. (2007). Localization of a stable neural correlate of associative memory. Science *317*, 1230–1233. https://doi.org/10.1126/science.1143839.
18. Zhou, X., Vink, M., Klaver, B., Berkhout, B., and Das, A.T. (2006). Optimization of the Tet-On system for regulated gene expression through viral evolution. Gene Ther. *13*, 1382–1390. https://doi.org/10.1038/sj.gt.3302780.
19. Braitenberg, V., and Schüz, A. (2013). Cortex: Statistics and Geometry of Neuronal Connectivity (Springer Science & Business Media).
20. Yadav, A., Gao, Y.Z., Rodriguez, A., Dickstein, D.L., Wearne, S.L., Luebke, J.I., Hof, P.R., and Weaver, C.M. (2012). Morphologic evidence for spatially clustered spines in apical dendrites of monkey neocortical pyramidal cells. J. Comp. Neurol. *520*, 2888–2902. https://doi.org/10.1002/cne.23070.
21. Yang, G., Pan, F., and Gan, W.B. (2009). Stably maintained dendritic spines are associated with lifelong memories. Nature *462*, 920–924. https://doi.org/10.1038/nature08577.
22. Moczulska, K.E., Tinter-Thiede, J., Peter, M., Ushakova, L., Wernle, T., Bathellier, B., and Rumpel, S. (2013). Dynamics of dendritic spines in the mouse auditory cortex during memory formation and memory recall. Proc. Natl. Acad. Sci. USA *110*, 18315–18320. https://doi.org/10.1073/pnas.1312508110.
23. Fu, M., Yu, X., Lu, J., and Zuo, Y. (2012). Repetitive motor learning induces coordinated formation of clustered dendritic spines in vivo. Nature *483*, 92–95. https://doi.org/10.1038/nature10844.
24. Dunsmoor, J.E., Niv, Y., Daw, N., and Phelps, E.A. (2015). Rethinking extinction. Neuron *88*, 47–63. https://doi.org/10.1016/j.neuron.2015.09.028.
25. Hortal, J., and Santos, A.M.C. (2020). Rethinking extinctions that arise from habitat loss. Nature *584*, 194–196. https://doi.org/10.1038/d41586-020-02210-x.
26. Lai, C.S.W., Adler, A., and Gan, W.B. (2018). Fear extinction reverses dendritic spine formation induced by fear conditioning in the mouse auditory cortex. Proc. Natl. Acad. Sci. USA *115*, 9306–9311. https://doi.org/10.1073/pnas.1801504115.
27. Hedrick, N.G., Lu, Z., Bushong, E., Singhi, S., Nguyen, P., Magaña, Y., Jilani, S., Lim, B.K., Ellisman, M., and Komiyama, T. (2022). Learning binds new inputs into functional synaptic clusters via spinogenesis. Nat. Neurosci. *25*, 726–737. https://doi.org/10.1038/s41593-022-01086-6.
28. Govindarajan, A., Kelleher, R.J., and Tonegawa, S. (2006). A clustered plasticity model of long-term memory engrams. Nat. Rev. Neurosci. *7*, 575–583. https://doi.org/10.1038/nrn1937.
29. McHugh, T.J., Blum, K.I., Tsien, J.Z., Tonegawa, S., and Wilson, M.A. (1996). Impaired hippocampal representation of space in CA1-specific NMDAR1 knockout mice. Cell *87*, 1339–1349. https://doi.org/10.1016/s0092-8674(00)81828-0.
30. Sheffield, M.E., and Dombeck, D.A. (2019). Dendritic mechanisms of hippocampal place field formation. Curr. Opin. Neurobiol. *54*, 1–11. https://doi.org/10.1016/j.conb.2018.07.004.
31. Govindarajan, A., Israely, I., Huang, S.Y., and Tonegawa, S. (2011). The dendritic branch is the preferred integrative unit for protein synthesis-dependent LTP. Neuron *69*, 132–146. https://doi.org/10.1016/j.neuron.2010.12.008.
32. Schneider, C.A., Rasband, W.S., and Eliceiri, K.W. (2012). NIH Image to ImageJ: 25 years of image analysis. Nat. Methods *9*, 671–675. https://doi.org/10.1038/nmeth.2089.
33. Dombeck, D.A., Harvey, C.D., Tian, L., Looger, L.L., and Tank, D.W. (2010). Functional imaging of hippocampal place cells at cellular resolution during virtual navigation. Nat. Neurosci. *13*, 1433–1440. https://doi.org/10.1038/nn.2648.
34. Pnevmatikakis, E.A., and Giovannucci, A. (2017). NoRMCorre: an online algorithm for piecewise rigid motion correction of calcium imaging data. J. Neurosci. Methods *291*, 83–94. https://doi.org/10.1016/j.jneumeth.2017.07.031.
35. Thévenaz, P., Ruttimann, U.E., and Unser, M. (1998). A pyramid approach to subpixel registration based on intensity. IEEE Trans. Image Process. *7*, 27–41. https://doi.org/10.1109/83.650848.

STAR★METHODS

KEY RESOURCES TABLE

REAGENT or RESOURCE	SOURCE	IDENTIFIER
Bacterial and virus strains		
AAV2/1-Fos-rtTA	Choi et al.[8]	N/A
AAV2/1-CamKII-iCre	Choi et al.[8]	N/A
AAV2/1-EF1a-DIO-myriRFP670V5-P2A-post-eGRASP	Choi et al.[8]	N/A
AAV2/1-TRE3G-myrmScarlet-I	This paper	N/A
AAV2/1-CamKII-cyan pre-eGRASP	Choi et al.[8]	N/A
AAV2/1-TRE3G-yellow pre-eGRASP	Choi et al.[8]	N/A
Chemicals, peptides, and recombinant proteins		
Heparin-Agarose	Sigma-Aldrich	H6508
Doxycycline hyclate	Sigma-Aldrich	D9891
Experimental models: Organisms/strains		
Mouse: C57BL/6 N	Samtako. Bio. Korea	N/A
Recombinant DNA		
pAAV-Fos-rtTA	Choi et al.[8]	Addgene 120309
pAAV-CamKII-iCre	Choi et al.[8]	N/A
pAAV-EF1a-DIO-myriRFP670V5-P2A-post-eGRASP	Choi et al.[8]	Addgene 111585
pAAV-TRE3G-myrmScarlet-I	This paper	N/A
pAAV-CamKII-cyan pre-eGRASP	Choi et al.[8]	Addgene 111586
pAAV-TRE3G-yellow pre-eGRASP	Choi et al.[8]	N/A
Software and algorithms		
IMARIS	Bitplane	https://imaris.oxinst.com/
Prism 9	GraphPad	https://www.graphpad.com/
MATLAB	MathWorks	https://kr.mathworks.com/
Video Freeze	Med Associates	https://www.med-associates.com/
FV30S-SW	Olympus	https://www.olympus-lifescience.com/
FV30S-DT	Olympus	https://www.olympus-lifescience.com/
ImageJ	Schneider et al.[32]	https://imagej.nih.gov/ij/
Other		
FVMPE-RS (two-photon excitation laser scanning microscope)	Olympus	https://www.olympus-lifescience.com/

RESOURCE AVAILABILITY

Lead contact

Further information and requests for resources and reagents should be directed to and will be fulfilled by the lead contact, Bong-Kiun Kaang (kaang@snu.ac.kr).

Materials availability

All the materials used in this study are available upon request.

Data and code availability

- Data reported in this paper will be shared by the lead contact upon request.
- This paper does not report original code.
- Any additional information required to reanalyze the data reported in this paper is available from the lead contact upon request.

EXPERIMENTAL MODEL AND SUBJECT DETAILS

Mice

All experiments were performed on 8-11-week-old male C57BL/6N mice purchased from Samtako. Bio. Korea. Mice were raised in 12-hr light/dark cycle in standard laboratory cages and given ad libitum access to food and water. All procedures and animal care followed the regulation and guidelines of the Institutional Animal Care and Use Committees (IACUC) of Seoul National University.

METHOD DETAILS

AAV virus production

In all experiments, we used Adeno-Associated Viruses serotype 1/2 that contains capsids of serotypes 1 and 2. The preparation of AAV1/2 was done as described previously.[11] HEK293T cells were cultured in 150 mm culture dishes and grown to ~60% confluency on the following day. Each dish was cultured in 18 ml of Opti-MEM (Gibco-BRL/Invitrogen, cat# 31985070) after being transfected with plasmids encompassing the vector of interest, AAV2 ITRs, p5E18, p5E18-RXC1, and pAd-F6. Five days after transfection, the supernatant media containing virus particles was transferred to a 50-ml tube and centrifuged at 3,000 rpm for 10 min. The supernatant was slowly added onto a poly-prep chromatography column (Bio-Rad Laboratories, cat# 731-1550) containing 1 ml of heparin-agarose suspension (Sigma, cat# H6508). To wash the column, 4 ml of Buffer 4-150 (150 mM NaCl, 10 mM citrate, pH 4.0) and 12 ml of Buffer 4-400 (400 mM NaCl, 10 mM citrate, pH 4.0) were used. The AAV1/2 particles were eluted by 4 ml of Buffer 4-1200 (1.2 M NaCl, 10 mM citrate, pH 4.0). The elute was loaded onto the Amicon Ultra-15 filter unit (Millipore, cat# UFC910024) and centrifuged at 4,000 rpm for 20 min. The AAV1/2 particles stuck in filter were eluted by adding 4 ml DPBS and centrifuging 4,000 rpm for 50 min. The titration of virus particles was done by quantitative RT-PCR.

Stereotaxic surgery

Adult 8-10-week-old WT mice were used for stereotaxic surgery and further experiments. For stereotaxic surgery, mice were anesthetized by i.p. injection of a ketamine/xylazine solution. Virus mixture was injected with a Hamilton syringe, using a 31-gauge needle. The needle was slowly lowered 0.05mm below the injection site for 2 min. After the needle was returned to the injection site, 0.5 μl of the virus mixture was injected at a rate of 0.125 μl/min. Following a 6-min wait for viral dispersion at the injection site and to prevent backflow, the needle was slowly withdrawn from the skull. Stereotaxic coordinates from bregma were: Right hippocampal CA1 (AP: -1.8 / ML: -1.45 / DV: -1.65 from dura), Left hippocampal CA3 (AP: -1.7 / ML: +2.35 / DV: -2.4). The concentrations of injected viruses are described in Table S1.

Hippocampal window surgery

For *in vivo* imaging experiments, we used 8–11-week-old male WT mice and implanted hippocampal window above dorsal CA1 of mice a week after virus injection surgery. Mice were fixed to a stereotactic frame after being given an intraperitoneal injection of ketamine / xylazine for anesthesia. Chronic hippocampal windows were implanted as described previously.[33] Briefly, a 2.7-mm diameter trephine drill (FST) was used to make a craniotomy at AP -2.0 mm, ML +1.8 mm from the bregma, covering the dorsal hippocampus. The cortical tissue above the CA1 area was carefully removed by aspiration after the dura was properly removed with forceps. By using Meta-Bond (Parkell), a customized stainless-steel cylindrical cannula with a 2.5-mm Ø round glass coverslip (Marienfeld, custom order) attached at the bottom was inserted and cemented to the skull. Chronic cranial windows were implanted over the dorsal CA1 at AP -1.8 mm, ML -1.45 mm from the bregma. The craniotomy was covered with a 2.5-mm spherical glass coverslip and sealed with Meta-Bond. Before the Meta-Bond was cured, a customized stainless-steel head ring was placed around either the cannula or the window and fixed with additional Meta-Bond.

Contextual fear conditioning and extinction

Each mouse was single caged immediately after the hippocampal window implant surgery. Before day-1 imaging, each mouse was habituated to the anesthesia chamber without isoflurane for 3 minutes on 5 consecutive days. Mice were conditioned on the next day of day-1 imaging. Two hours before conditioning, 100 μg/g doxycycline was injected by i.p. injection during brief anesthesia by isoflurane in the anesthesia chamber. Conditioning sessions were 300 sec in duration, and three 0.75 mA shocks of 2 s duration were delivered at 208 s, 238 s, and 268 s in a square chamber with a steel grid (Med Associates, St Albans, VT). When the contextual fear conditioning was finished, mice were immediately transferred to their homecage. Two days after conditioning, day-2 imaging was performed. On the following day, extinction groups were exposed to the conditioned context for 3 consecutive days, whereas no extinction group stayed at homecage. After day-6 imaging, mice were exposed to the same context to measure freezing levels and were perfused for immunohistochemistry.

Sample preparation and confocal imaging

Mice were deeply anaesthetized with a ketamine/xylazine solution and perfused with PBS and PBS with 4% paraformaldehyde (PFA). The implanted hippocampal window in the brain was carefully removed, and the brain was further fixed with 4% PFA solution overnight at 4°C. The brain was dehydrated in PBS with 30% sucrose for 2 days at 4°C. The brain was frozen and sliced with a cryostat in 40 μm sections for immunohistochemistry or 50 μm for confocal imaging. Brain slices were mounted with VECTASHIELD mounting

medium (Vector Laboratories). For dual-eGRASP imaging, dendrites in CA1 stratum radiatum were imaged in Z-stack with Leica SP8 confocal microscope with 63x distilled water immersion objective lens.

In vivo two-photon imaging

The dorsal CA1 was imaged through the hippocampal window using a two-photon excitation laser scanning microscope (Olympus, FVMPE-RS). The two-photon microscope was equipped with four photomultiplier tubes, a Ti:Sapphire laser (Mai-Tai DeepSee, Spectra-Physics), a galvo/resonant scanner, and a 25× 0.95 NA water immersion objective with an 8-mm working distance (Olympus, XLSLPLN25XSVMP2). Excitation wavelengths of 880 nm (for Cyan GRASP and iRFP imaging) and 960 nm (for Yellow GRASP and mScarlet-i imaging) were used. Cyan GRASP and Yellow GRASP fluorescence were reflected by a long-pass dichroic mirror (Olympus, FV30-SDM570), followed by passing a filter cube (Olympus, FV30-FCY) that consisted of a 505 nm long-pass dichroic mirror, 460-500 nm band-pass filter, and 520-560 nm band-pass filter. mScarlet-i and iRFP signal were collected after passing through a filter cube (Olympus, FV30-FRCY5) that consist of 650 nm long-pass dichroic mirror, 575-645 nm band-pass filter, and 660-750 nm band-pass filter. To reduce motion artifacts, we collected 30 images for each z-plane using a resonant scanner that has a 30 Hz image acquisition rate. In each area, we scanned 84.8 μm× 84.8 μm× 30 μm before fear conditioning and 84.8 μm× 84.8 μm× 32 μm after fear conditioning. During two-photon imaging, mice were anesthetized by isoflurane inhalation using a low-flow vaporizer (Kent Scientific, SomnoSuite), and the body temperature was maintained at 37 °C.

Image processing

For synapse-level two-photon imaging, it was critical to correct for motion artifacts due to cardiac and respiratory rhythms. 30 images for each z-stack acquired with resonant/galvo scanner were motion corrected with NoRMCorre[34] package on MATLAB 2021a. After averaging the images at each z-plane, four channel images from 880 nm and 960 nm excitation were aligned by MultiStackReg plugin[35] on Image J.[32] Deconvolution of two-photon microscopy images was performed by using the Parallel Iterative Deconvolution plugin on Image J.[32]

IMARIS analysis

Imaris (Bitplane, Zurich, Switzerland) software was used to process and analyze the two-photon images. Each trackable myr_mScarlet-I-positive or myr_iRFP670-only dendrites were manually denoted as engram or non-engram dendrites by a researcher, while other researchers were blinded from the information during analysis. Each cyan or yellow eGRASP signal was manually denoted with the annotation tool within Imaris. When the cyan and yellow eGRASP signals overlapped in a single synapse, it was denoted as overlapping annotations as the presynaptic neuron of the synapse indicating IEG-positive during memory formation. The length of each dendrite on day-1 and day+2 was calculated using Imaris measurement and was averaged. For relative density analysis, cyan and yellow eGRASP density of each dendrite was normalized to the average spine density of the cyan and yellow eGRASP on the myr_iRFP670-only dendrites, respectively. In all IMARIS analysis, the investigators who analyzed the images were blinded to the behavior group of mice.

Spine distribution analysis

For spine distribution analysis, coordinates of all denoted spots and their labels were used to calculate distance between spines in the custom MATLAB code. To evaluate the density of surrounding spines in Figure 4D, we first calculated the first principal component vector using the coordinate of all spines on the dendrite segment. By projecting the spines on the principal vector line, we generated a one-dimensional spine map. To calculate the density of spine, we binned the spine location every 0.06 μm, and filtered it with a gaussian window of 2.5 μm standard deviation.

QUANTIFICATION AND STATISTICAL ANALYSIS

Data analysis and figures were prepared using Prism software. To analyze GRASP data that was not normally distributed, the Mann-Whitney test was used. The value of n and statistical significance were described in each figure legends.